



Contents lists available at ScienceDirect

CIRP Journal of Manufacturing Science and Technology

journal homepage: [www.elsevier.com/locate/cirpj](http://www.elsevier.com/locate/cirpj)



## Improved chip thickness model for serrated end milling

Pritam Bari<sup>a</sup>, Mohit Law<sup>a,\*</sup>, Pankaj Wahi<sup>b</sup>

<sup>a</sup> Machine Tool Dynamics Laboratory, Department of Mechanical Engineering, Indian Institute of Technology Kanpur, Kanpur 208016, India

<sup>b</sup> Department of Mechanical Engineering, Indian Institute of Technology Kanpur, Kanpur 208016, India

### ARTICLE INFO

Article history:  
Available online xxx

**Keywords:**  
Cutting  
Tool path  
Trochoid  
Serrated  
End milling  
Chip thickness

### ABSTRACT

This paper presents an improved chip thickness model for serrated end mills that accounts for the actual trochoidal path traced by the tooth. The model includes the influence of radial run-out on teeth. We also present a method to infer radial run-out on serrated tools using a combination of measurements and scanned geometry of the serration profiles. We present results for cutters with serrations of the trapezoidal and circular kinds. We observe differences in chip thickness and cutting forces evaluated using the proposed model and with those evaluated using a circular tool path approximation to increase with feed and radial engagements. However, the differences are negligible, being at most 2%, suggesting that the circular chip thickness model is indeed a reasonable approximation for predicting cutting forces with serrated cutters. Experiments confirm predictions. For run-outs of the order of feed, i.e., 0.02–0.05 mm/tooth/rev, or less, we find that cutting force profiles and levels are not significantly altered. The resultant force with moderate levels of run-out included in the model is at most 1% different than the case without run-out, suggesting that serrated cutters may be used even with moderate levels of run-outs when the feed is low. Results can instruct the design and use of serrated cutters that reduce forces and make easier the high-performance machining of difficult-to-cut materials across industries.

© 2019 CIRP.

### Introduction

Chip thickness and force models are a function of the path traced by the milling cutter, which in reality is that of an arc of a trochoid, and not circular, as has been customarily assumed. What role, if any, does this trochoidal path play in chip thickness models for serrated cutters is less understood. Understanding this is important in the case of serrated cutters, since serrations along the cutting edges change the local radius. This change results in a continuously varying non-uniform chip thickness that may result in the apparent depth of cut to be less than the actual depth of cut – which contributes to a reduction in cutting forces for cutting with serrated tools.

To instruct the design of better serrated cutters that can further reduce forces and make easier the high-performance machining of difficult-to-cut materials across industries, it is hence necessary to understand the influence of the real path traced by the cutting edge. This is the main focus of this paper. Further, what role, if any, does any potential run-out on the serrated cutter have on the chip thickness/force model, is also less understood, and will also be addressed in this paper.

Seminal early work on milling processes by Martellotti [1,2] had showed that due to a combination of the translational motion of the cutter/workpiece and the rotary motion of tool, the path traced by the tooth is that of a trochoid, and that this results in the local tooth geometry, chip thickness, and force to continuously change with position and the radius of curvature of the tooth path. Later developments that considered trochoidal paths improved upon chip thickness models to make them implementation friendly [3,4]. Further improvements were proposed in [5,6] that also modelled the change in chip thickness for variable pitch cutters with run-outs [7]. Others extended modelling with trochoidal tool paths to ball end milling [8], and to also the case of dynamically predicting surface topographies for milling of flexible parts [9,10].

The literature addressing the influence of trochoidal chip thickness in milling has focused only on regular end mills, wherein it was reported that during normal milling the feed rate used is very low with respect to local radius of the tool, and hence trochoidal chip thickness does not have any significant effect in the predicted forces with respect to conventional circular chip thickness, except for the case of micro-milling operations [11]. How, if, at all, the actual trochoidal tooth path changes the chip thickness and forces for serrated end mills, is yet unknown.

Research on modelling serrated end mill geometry has all assumed the tooth path to be approximately circular. The work was concerned with either explaining the reduced contact between the

\* Corresponding author.  
E-mail address: [mlaw@iitk.ac.in](mailto:mlaw@iitk.ac.in) (M. Law).

tool and the workpiece as the reason for reducing cutting forces [12], or with presenting good generalized mechanics based geometric models for serrated cutters that could explain the change in local radius and the variation of local tool angles along the serration profiles [13–18], or with optimizing serration profiles for reducing forces [19,20]. Earlier work on serrated end milling did not consider the actual trochoidal tooth path, nor did it include the influence of run-out on chip thickness models for serrated cutters, even with circular tooth path approximations.

Run-out, though undesirable, is invariably present on tools. Its presence changes the nature of local chip thickness and forces which contributes to premature tool wear and breakage. Modelling its influence on regular tools has hence received some attention, with a focus on understanding its effect on force profiles in end mills [7] and face mills [21], or on its influence on cutting force coefficient identification [22] and surface topographies [23,24], or even in five-axis milling processes [25]. Studies [26,27] have also investigated the adverse influences of run-out on the dynamic displacements during ball-end milling of inclined surfaces. Understanding, how, if, at all, the run-out changes the local chip thickness and force profiles for serrated cutters with trochoidal and/or circular tooth paths remains unaddressed.

Since serrated cutters preferentially reduce cutting forces, the influence of trochoidal chip thickness on cutting forces, and the influence of run-out on force profiles, needs to be understood comprehensively based on systematic model based investigations, and is the main motivation of the present work. We limit our discussions in this paper to serrations only of the trapezoidal and circular kind. We ignore axial run-out, and assume that only radial run-out exists on serrated tools. Measuring run-out on regular end mills is possible, and has been reported elsewhere, see for example [28–30]. However, measuring run-out on serrated cutters due to the constantly changing radius along the serration is non-trivial, which is addressed in our paper.

At first, we present an expanded geometric model for serrated cutters including run-out. Thereafter, the trochoidal chip thickness model with run-out is presented, following with the force model is discussed. After which, we systematically investigate the difference between conventional circular chip thickness and the actual trochoidal chip thickness, and the corresponding differences in cutting forces. We present results with and without run-out for a wide range of cutting operating parameters. The procedure for measurement of run-out parameters for serrated cutters is also explained. Following which, experimental validation is presented, followed by the main conclusions.

### Geometric model of serrated cutter

This section describes the geometry of serrated cutters that lead to a preferential reduction in cutting forces. At first, local geometries are defined considering the influence of run-out, followed by describing a generalized method to model serrations, followed by discussions on multiple delays caused by serrations. Models described here are based on the classic work done by Merdol and Altintas [15] and Dombovari et al. [16] and also on our own earlier reported work [31,32].

### Defining local radius and geometry

A schematic, and a cross-sectional view of a serrated cutter with run-out is shown in Fig. 1. Due to the run-out, cutter geometrical centre, denoted by  $O_g$  deviates from spindle rotation centre, by a constant radial deviation,  $\mu$ . The run-out angle between the direction of radial offset (deviation) and the nearest tooth at the bottom of the tool is denoted by  $\delta$ . We assume that there is no axial run-out or any cutter geometric axis tilt, i.e.  $\mu$  is constant along the

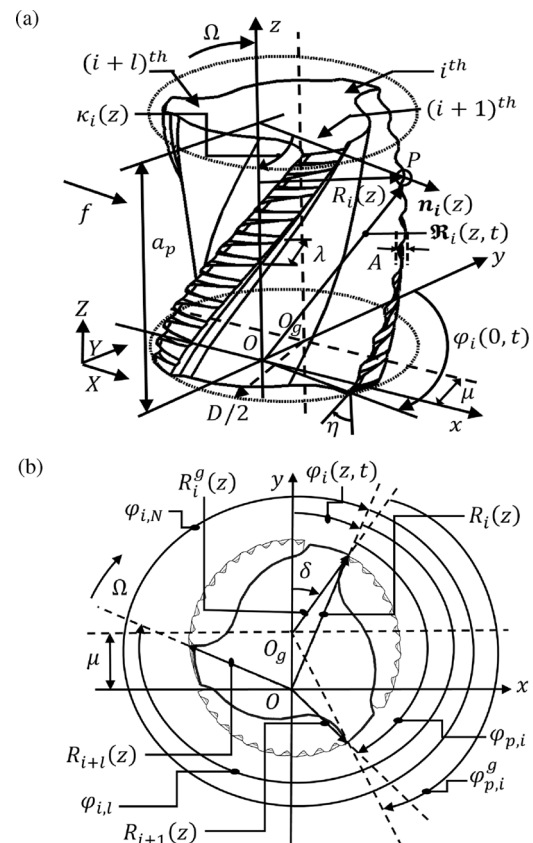


**Fig. 1.** (a) Geometry of the serrated cutter with run-out (b) Cross-sectional view at height  $z$  with run-out.

cutter height. Due to the run-out, since the whole system rotates about the spindle axis through  $O$ , it is convenient to model all things with respect to  $O$ , and hence the  $xyz$  coordinate frame is attached to the tool at  $O$  as shown in Fig. 1a.  $xyz$  is a non-rotating body fixed co-ordinate system moving along with the tool in the  $x$ -direction at a feed of  $f$  mm/tooth/rev with respect to the global inertial frame  $XYZ$ .

The cutter can have  $N$  number of flutes (teeth), but as an example, only three ( $i^{th}$ ,  $(i+1)^{th}$  and  $(i+l)^{th}$ ) flutes are shown in Fig. 1. Serrations change the local geometrical radius along the flute and the height. The local geometrical radius  $R_z^g(z)$ , measured with respect to the geometrical axis (dashed line through  $O_g$  shown in Fig. 1 a), is parallel to the  $z$ -axis for the  $i^{th}$  flute at the height  $z$ , and is defined as:

$$R_i^g(z) = \frac{D}{2} - \Delta R_i^g(z), \quad (1)$$

wherein  $D$  is shank diameter of the cutter, and  $\Delta R_z^g(z)$  is the variation in local radius. Geometry is to be measured with respect to the spindle rotational axis that does not align with the cutter's geometrical axis due to eccentricity between them caused by the run-out. Due to the run-out, we define another local radius called the rotational radius with respect to the  $z$ -axis through  $O$  as follows:

$$R_i(z) = \left[ \left( \mu + R_i^g(z) \cos \left( \delta - \sum_{k=1}^{i-1} \varphi_{p,k}^g - \frac{2z \tan \eta}{D} \right) \right)^2 + \left( R_i^g(z) \sin \left( \delta - \sum_{k=1}^{i-1} \varphi_{p,k}^g - \frac{2z \tan \eta}{D} \right) \right)^2 \right]^{0.5}, \quad (2)$$

wherein  $\varphi_{p,i}^g(z)$ , the pitch angle, is the angle between the  $i^{th}$  and the  $(i+1)^{th}$  flute in the  $x-y$  plane, and  $\eta_i(z)$  is the helix angle. When the run-out is low with respect to geometrical radius, i.e.,  $\mu \ll R_i^g(z)$ , which is usually the case, Eq. (2) can be linearized to the following simplified form:

$$R_i(z) = R_i^g(z) + \mu \cos\left(\delta - \sum_{k=1}^{i-1} \varphi_{p,k}^g - \frac{2z \tan \eta}{D}\right). \quad (3)$$

In addition to causing a change in the local radius, run-out also changes the instantaneous radial immersion angle. The angular position for the  $i^{th}$  flute at height  $z$ , measured clockwise from the  $y$  axis in the  $x-y$  plane considering the run-out, called the instantaneous radial immersion angle, is calculated as follows:

$$\varphi_i(z, t) = \Omega t + \sum_{k=1}^{i-1} \varphi_{p,k} - \frac{2z \tan \eta}{D}, \quad (4)$$

wherein  $\Omega$  is the clockwise spindle speed (rad/s) and  $\varphi_{p,i}$  is the new pitch angle with respect to  $O$  due to the run-out. The relationship between the new pitch angle  $\varphi_{p,i}$  with respect to  $O$  and the geometrical pitch angle  $\varphi_{p,i}^g$  with respect to  $O_g$  is shown in Fig. 2. From Fig. 2, using the cosine triangle formula,  $\varphi_{p,i}$  is calculated as follows:

$$\varphi_{p,i} = \cos^{-1} \frac{(R_i(z))^2 + (R_{i+1}(z))^2 - (L_i(z))^2}{2R_i(z)R_{i+1}(z)}, \quad (5)$$

wherein  $L_i(z) = \sqrt{(R_i^g(z))^2 + (R_{i+1}^g(z))^2 - 2R_i^g(z)R_{i+1}^g(z)\cos\varphi_{p,i}^g}$ .

When the tool rotates at a speed  $\Omega$  then the position vector (measured from the origin  $O$ ) of an element  $P$  located in the  $i^{th}$  cutting edge at the height  $z$  is defined as:

$$\mathbf{R}_i(z, t) = R_i(z)\sin\varphi_i(z, t)\vec{i} + R_i(z)\cos\varphi_i(z, t)\vec{j} + z\vec{k}, \quad (6)$$

wherein  $R_i(z)$  is the local radius in the  $x-y$  plane and  $\varphi_i(z, t)$  is the angular position of the point  $P$  calculated from Eqs. (3) and (4).

Due to the changing local radius, an axial immersion angle (lead angle)  $\kappa_i(z)$ , which is the angle between the  $z$ -axis of the cutter and the normal vector  $\mathbf{n}_i(z)$  to local flute tangent at the point  $P$ , as shown in the Fig. 1b, also forms part of the force computations, and is expressed by:

$$\cot\kappa_i(z) = \frac{dR_i(z)}{dz}. \quad (7)$$

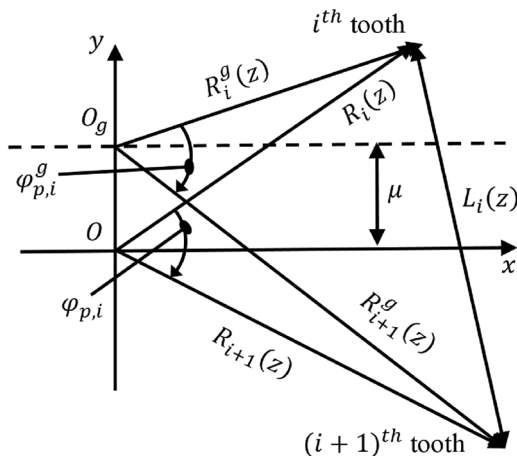


Fig. 2. Calculation of the new rotational pitch angle,  $\varphi_{p,i}$  due to the run-out on serrated cutters.

Having defined the local radius and geometry, for the sake of completeness, we now draw attention to modelling different types of serration profiles.

#### Defining serration profiles

The variation in local radius  $\Delta R_i^g(z)$  defined in Eq. (1), is evaluated from an imagined extended outer surface of a cylinder over the flute portion shown in Fig. 3.  $\Delta R_i^g(z)$  depends on the type of the serration profile, which can be sinusoidal, trapezoidal, circular, or of some other form. The two important parameters describing any serration profile are the amplitude ( $A$ ) and the wavelength ( $\lambda$ ), with the profile repeating with  $\lambda$ . There is also a phase shift ( $\psi_i$ ) between the starting of the serration profile on each flute, which can be described as:

$$\psi_i = \sum_{k=1}^{i-1} \varphi_{p,k}, \quad (8)$$

wherein  $\varphi_{p,k}$  is the pitch angle between the  $k^{th}$  and  $(k+1)^{th}$  flute, and  $\psi_1 = 0$ .

As the flutes are inclined to the  $z$ -axis by the helix angle, we define a direction along the tangent of the cutting edge flute called the  $s$ -direction shown in Fig. 3. The parameter  $s$  is expressed in terms of  $\lambda$  and  $z$  as follows:

$$s = \text{rem}\left(\frac{\chi}{\lambda}\right), \quad (9)$$

wherein  $\chi = \frac{z}{\cos\eta_i(z)} - \frac{\lambda\psi_i}{2\pi}$  and  $\chi = \chi + \lambda$  when  $\chi < 0$ .

As the serration profile is along  $s$  direction, the variation of local radius  $\Delta R_i^g(z)$  defined in Eq. (1) is replaced by an equivalent term  $R_i^s(s)$ , where the value of  $s$  is calculated corresponding to  $z$  values using Eq. (9). The expression of  $R_i^s(s)$  for the serration profiles of interest in this paper, i.e., the trapezoidal and the circular profiles are discussed next.

#### Trapezoidal serration profile

The trapezoidal profile is defined as shown in Fig. 4. There is one upper land of length  $L_1$ , one lower land of length  $L_2$ , and two inclined lands with inclination angles  $\alpha_{serr}$  and  $\beta_{serr}$ . The serration profile also consists of four small arcs of circles of radii  $R_1, R_2, R_3$  and  $R_4$ .

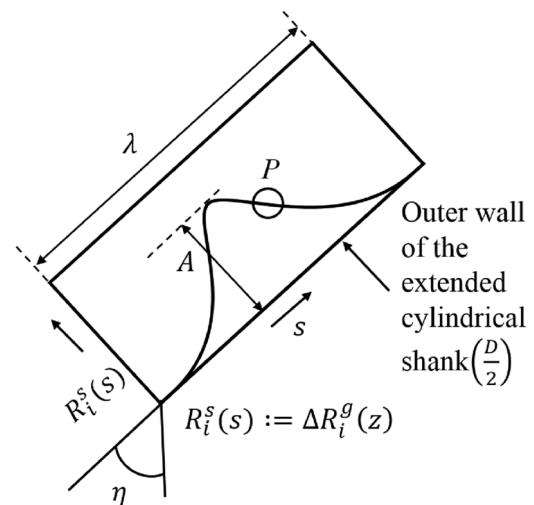


Fig. 3. Serration profile along  $s$ -direction (along the edge of inclined flute).

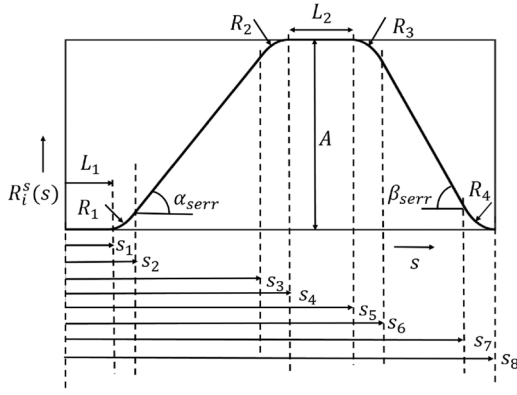


Fig. 4. Schematic of trapezoidal serration profile.

The variation in local radius  $R_i^s(s)$  for the trapezoidal serration profile is given by:

$$\left. \begin{aligned} &\text{if } 0 \leq s < s_1, \\ &R_i^s(s) = 0 \\ &\text{if } s_1 \leq s < s_2, \\ &R_i^s(s) = R_1 - \sqrt{R_1^2 - (s - s_1)^2} \\ &\text{if } s_2 \leq s < s_3, \\ &R_i^s(s) = R_1 - \sqrt{R_1^2 - (s_1 - s_2)^2} + \tan \alpha_{serr}(s - s_2) \\ &\text{if } s_3 \leq s < s_4, \\ &R_i^s(s) = A - R_2 + \sqrt{R_2^2 - (s - s_4)^2} \\ &\text{if } s_4 \leq s < s_5, \\ &R_i^s(s) = A \\ &\text{if } s_5 \leq s < s_6, \\ &R_i^s(s) = A - R_3 + \sqrt{R_3^2 - (s - s_5)^2} \\ &\text{if } s_6 \leq s < s_7, \\ &R_i^s(s) = R_4 - \sqrt{R_4^2 - (s_7 - s_8)^2} - \tan \beta_{serr}(s - s_7) \\ &\text{if } s_7 \leq s \leq s_8, \\ &R_i^s(s) = R_4 - \sqrt{R_4^2 - (s - s_8)^2} \end{aligned} \right\}, \quad (10)$$

wherein

$$\left. \begin{aligned} s_1 &= L_1 \\ s_2 &= s_1 + R_1 \sin \alpha_{serr} \\ s_3 &= s_2 + (A - (R_2 + R_1)(1 - \cos \alpha_{serr})) \cot \alpha_{serr} \\ s_4 &= s_3 + R_2 \sin \alpha_{serr} \\ s_5 &= s_4 + L_2 \\ s_6 &= s_5 + R_3 \sin \beta_{serr} \\ s_7 &= s_6 + (A - (R_3 + R_4)(1 - \cos \beta_{serr})) \cot \beta_{serr} \\ s_8 &= s_7 + R_4 \sin \beta_{serr} \\ \lambda &= s_8 \end{aligned} \right\}. \quad (11)$$

#### Circular serration profile

The circular serration profile is defined as shown in Fig. 5. There are two arcs of circles of radii  $R_1$  and  $R_2$  centered at  $O_1$  and  $O_2$  with arc heights  $A_1$  ( $< R_1$ ) and  $A_2$  ( $< R_2$ ).

The variation in local radius  $R_i^s(s)$  for circular serration is given by:

$$\left. \begin{aligned} &\text{if } 0 \leq s < s_1 \\ &R_i^s(s) = R_1 - \sqrt{R_1^2 - \left(s - \frac{s_1}{2}\right)^2} \\ &\text{if } s_1 \leq s \leq s_2 \\ &R_i^s(s) = A_1 + A_2 - R_2 + \sqrt{R_2^2 - \left(\frac{s_1 + s_2}{2} - s\right)^2} \end{aligned} \right\}, \quad (12)$$

wherein

$$\left. \begin{aligned} s_1 &= 2\sqrt{A_1(2R_1 - A_1)} \\ s_2 &= s_1 + 2\sqrt{A_2(2R_2 - A_2)} \\ \lambda &= s_2 \\ A &= A_1 + A_2 \end{aligned} \right\}. \quad (13)$$

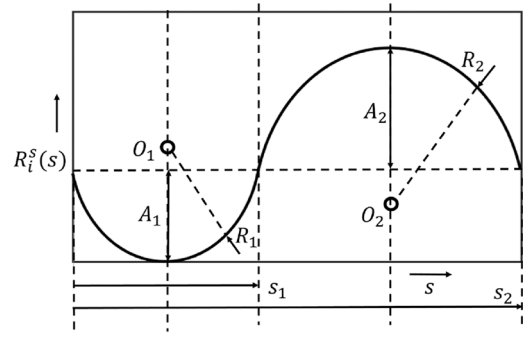


Fig. 5. Schematic of circular serration profile.

Having described methods to define serration profiles of interest, we address next, how a change in the local radius influences surface generation.

#### Multiple delays between serrated flutes

Due to the serration profile and changes in the local radius across the height of the cutter, it is possible that the cut surface generated previously, was made either by the same flute in the previous pass or by other flutes in same pass. This leads to multiple delays, where delay is the time elapsed between formation of the current surface being generated and the previous surface generated. If the current cut surface is made by  $i^{th}$  flute at time  $t$  and the previous cut surface was made by  $(i + l)^{th}$  flute at time  $t - \tau_{i,l}(z)$ , then at the same angular position one can rewrite the instantaneous radial immersion angle as (shown in Fig. 1b):

$$\varphi_i(z, t) = \varphi_{i+l}(z, t - \tau_{i,l}(z)), \quad (14)$$

wherein  $\tau_{i,l}$  is the multiple delay term for serrated cutter and it is defined as:

$$\tau_{i,l}(z) = \frac{\varphi_{i,l}(z)}{\Omega} = \frac{1}{\Omega} \sum_{k=1}^{l-1} \varphi_{p,(i+k) \bmod N}(z). \quad (15)$$

This delay is used in the estimation of the improved local chip thickness as discussed next.

#### Improved chip thickness model

The improved chip thickness model incorporates the trochoidal trajectory of the cutter [33]. A trochoid is the curve described by a fixed point  $P$  on a circle of radius  $r$  as it rolls along a straight line [34]. There are three types of trochoidal paths. If the point  $P$  lies inside the circle, on its circumference, or outside, then the trochoid is described as being curtate, common, or prolate, respectively. The value of  $r$  should be such that tangential velocity will be equal to the linear feed of the centre of the cutter, i.e., the pure rolling condition should be satisfied. For serrated end mills, the tangential velocity at the periphery of the teeth is much higher than the velocity of centre (rotational centre  $O$ , considering run-out) as the feed rate is much lower than the diameter of the cutter. Hence the imaginary circle will lie inside the cutter periphery, i.e.,  $r < R_i(z, t)$ . Hence all the flutes follow a prolate trochoid path when the cutter rotates at speed  $\Omega$  rad/sec and is fed in the  $x$ -direction at a feed of  $f$  mm/tooth/rev as shown in Fig. 6.

Along the circle of radius  $r$  we get  $\Omega r = \frac{\Omega}{2\pi} N f$ , where  $N$  is the number of flutes. Hence we get  $r = \frac{Nf}{2\pi}$  mm. Comparison of this trochoidal path with conventional circular path considering radial run-out is shown in Fig. 7. For circular path geometric radius ( $R$ ) and radius of curvature ( $\rho$ ) are the same, whereas for trochoidal



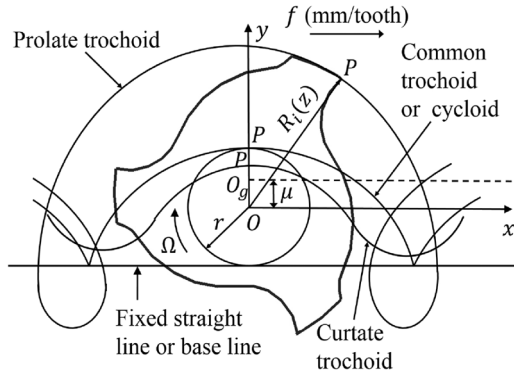


**Fig. 6.** Different types of trochoid paths traced by different points on the serrated cutter with run-out.

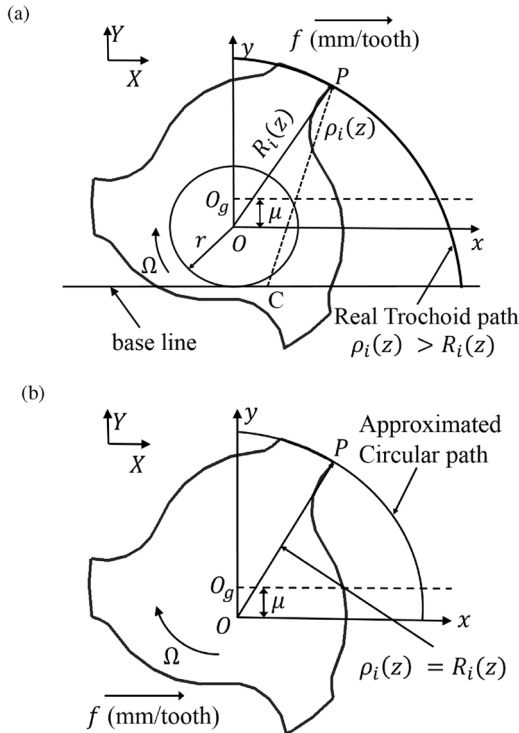


**Fig. 7.** Difference between (a) trochoid and (b) circular path considering run-out.

paths they are different, and the center of curvature always lies on the base line over which the inside circle rolls.

Since the cutter actually traces a trochoidal path, the radius of curvature for this path is obtained as described next.

#### Radius of curvature of trochoidal path

The position of the  $i^{\text{th}}$  flute at height  $z$  at time  $t$  (point  $P$ ) along the trochoidal path is described as follows:

$$P_i(z, t) = [X_i(z, t) \ Y_i(z, t)]^T = \begin{bmatrix} r\varphi_i(z, t) + R_i(z)\sin\varphi_i(z, t) \\ R_i(z)\cos\varphi_i(z, t) \end{bmatrix}. \quad (16)$$

Substituting  $Y_i(z, t)$  by  $[R_i(z) - d_i(z, t)]$  in Eq. (16), wherein  $d_i(z, t)$  is the instantaneous radial depth of cut as shown in Fig. 8 (more details of which are discussed nextSection 3.2), we obtain:

$$X_i(z, t) = r\cos^{-1}\left(\frac{R_i(z) - d_i(z, t)}{R_i(z)}\right) + [\{2R_i(z) - d_i(z, t)\}d_i(z, t)]^{0.5}. \quad (17)$$

From Eqs. (16) and (17) the slope to the trochoidal path is evaluated as follows:

$$\tan\phi_i(z, t) = \frac{dY_i(z, t)}{dX_i(z, t)} = \frac{\frac{dY_i(z, t)}{d\varphi_i(z, t)}}{\frac{dX_i(z, t)}{d\varphi_i(z, t)}} = \frac{-[\{2R_i(z) - d_i(z, t)\}d_i(z, t)]^{0.5}}{[r + R_i(z) - d_i(z, t)]}. \quad (18)$$

Radius of curvature of the trochoidal path followed by the tool teeth, which is measured from the rolling line (base line), is governed by the following expression [35]:

$$\rho_i(z, t) = \frac{\left[1 + \left(\frac{dY_i(z, t)}{dX_i(z, t)}\right)^2\right]^{\frac{3}{2}}}{\frac{d^2Y_i(z, t)}{dX_i^2(z, t)}}, \quad (19)$$

$$\text{wherein } \frac{dY_i(z, t)}{dX_i(z, t)} = \tan\phi_i(z, t) \text{ and } \frac{d^2Y_i(z, t)}{dX_i^2(z, t)} = \frac{d\left(\frac{dY_i(z, t)}{dX_i(z, t)}\right)}{dX_i(z, t)} = \frac{d\left(\frac{\tan\phi_i(z, t)}{d\varphi_i(z, t)}\right)}{d\varphi_i(z, t)}.$$

Using Eqs. (16)–(19) we finally obtain the following expression of radius of curvature:

$$\rho_i(z, t) = \frac{\left[\frac{fN}{\pi}(R_i(z) - d_i(z, t)) + R_i(z)^2 + \left(\frac{fN}{2\pi}\right)^2\right]^{\frac{3}{2}}}{-\frac{fN}{2\pi}(R_i(z) - d_i(z, t)) - R_i(z)^2}. \quad (20)$$

Eq. (20) is used to calculate the chip thickness as discussed next.

#### Trochoidal chip thickness for serrated cutters

Elemental geometric static chip thickness  $h_{g, \text{cir}}^{\text{st}}(z, t)$  of the serrated cutter with run-out considering circular approximation is defined as the local distance between the current surface and the next surface to be cut in the direction of normal vector  $\mathbf{n}_i(z)$  of the flute as:

$$h_{g, \text{cir}}^{\text{st}}(z, t) = \min_{l=1}^N [(R_i(z) - R_{i+l}(z)) + f_{i,l}(z, t)\sin\varphi_i(z, t)]\sin\kappa_i(z), \quad (21)$$

wherein  $f_{i,l}(z, t)$  is the corresponding feed motion during delay  $\tau_{i,l}$  between the  $i^{\text{th}}$  flute and the  $(i + l)^{\text{th}}$  flute and  $R_i(z)$  is rotational radius due to run-out calculated from Eq. (3). The first two terms in the right hand side of Eq. (21) are due to variation in local radius, and the last term is due to rotation and linear feed motion of the serrated cutter. Eq. (21) is derived considering conventional circular trajectories of the tooth. In reality tooth path trajectories are trochoidal. A schematic view of the chip thickness formation of the serrated cutter with run-out due to actual trochoidal tooth path trajectories is shown in Fig. 8.

Since the chip thickness is calculated using rotational radius, the eccentricity line through geometric centre  $O_g$  is not shown in Fig. 8 for brevity. Position of the centre of serrated cutter at seven different times:  $t_1 < t_2 < t_3 < t_4 < t_5 < t_6 < t_7$  are shown by:  $O_1, O_2, O_3, O_4, O_5, O_6, O_7$  points respectively in Fig. 8. Inner circles are drawn only at  $t_1$  and  $t_4$ . Assume that the current cut surface is made by the  $i^{\text{th}}$  flute and next surface to be cut is made by the  $(i + l)^{\text{th}}$  flute due to multiple delays of the serrated cutter. Positions of the  $i^{\text{th}}$  flute in the current surface at the time  $t_1, t_2, t_3$  and  $t_5$  are denoted by  $P_1^i, P_2^i, P_3^i$  and  $P_5^i$ , respectively. At time  $t_4, t_6$  and  $t_7$  the position of  $(i + l)^{\text{th}}$  flute in next surface to be cut (red colour thick dashed line) are denoted by  $P_4^{i+l}, P_6^{i+l}$  and  $P_7^{i+l}$  respectively. When the  $i^{\text{th}}$  flute is in between positions at times  $t_3$  and  $t_5$ , then the  $(i + l)^{\text{th}}$  comes into the cutting path at time  $t_4$ , as is evident in Fig. 8.

Radius of curvature  $\rho_i(z, t)$  and radius of geometry  $R_i(z)$  are drawn at instants of  $P_3^i$  and  $P_6^{i+l}$ . Corresponding center of curvatures

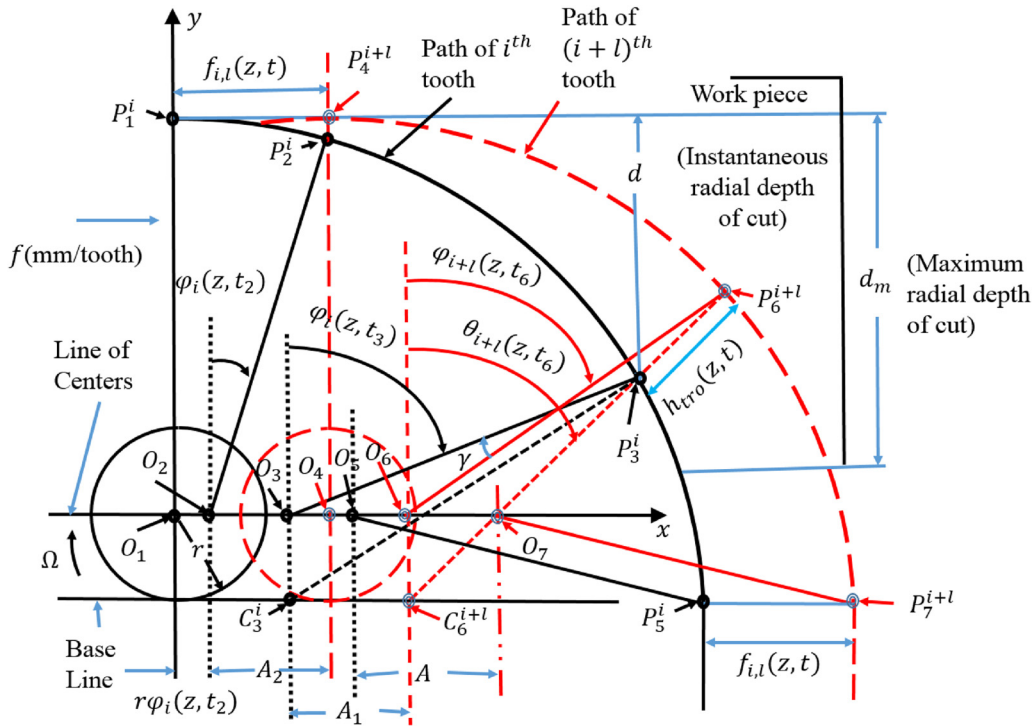


**Fig. 8.** Trochoidal chip thickness calculation for serrated cutter with run-out. The legends are as follows: the current surface (black colour thick solid line) made by the  $i^{th}$  flute; the next surface (red colour thick dashed line) made by the  $(i+l)^{th}$  flute; Geometric radius (solid line); Radius of curvature (thin dashed line).

are denoted by  $C_3^i$  and  $C_6^{i+l}$ . Hence we obtain  $P_6^{i+l}C_6^{i+l} = \rho_{i+l}(z, t_6)$ ;  $P_6^{i+l}O_6 = R_{i+l}(z)$   $P_3^iC_3^i = \rho_i(z, t_3)$  and  $P_3^iO_3 = R_i(z)$ . Considering trochoidal trajectories, the elemental trochoidal geometric static chip thickness is:

$$h_{g,tro}^{st}(z, t) = \min_{i=1}^N [(R_i(z) - R_{i+l}(z)) + h_{tro}(z, t)] \sin \kappa_i(z), \quad (22)$$

wherein  $h_{tro}(z, t)$  is the relative radial distance between two corresponding trochoidal trajectories along the radius of curvature shown in Fig. 8, and can be expressed as:

$$h_{tro}(z, t) = P_6^{i+l} - P_3^i = C_6^{i+l}P_6^{i+l} - C_6^{i+l}P_3^i = \rho_{i+l}(z, t_6) - C_6^{i+l}P_3^i. \quad (23)$$

The terms  $\rho_{i+l}(z, t_6)$  and  $C_6^{i+l}P_3^i$  in Eq. (23) are unknowns, and can be evaluated from the geometry in Fig. 8, wherein  $\Delta C_6^{i+l}P_3^iC_3^i$ ,  $P_3^iC_3^i = \rho_i(z, t_3)$  and  $C_3^iC_6^{i+l} = A_1$ . Assuming  $\angle C_6^{i+l}P_3^iC_3^i = \varepsilon$ , and using the sine rule for  $\Delta C_6^{i+l}P_3^iC_3^i$ , we can write:

$$\frac{C_6^{i+l}P_3^i}{\sin\{\pi - (\theta_{i+l}(z, t_6) + \frac{\pi}{2} + \varepsilon)\}} = \frac{\rho_i(z, t_3)}{\sin(\theta_{i+l}(z, t_6) + \frac{\pi}{2})} = \frac{A_1}{\sin \varepsilon}. \quad (24)$$

From Eq. (24) we can derive the following two equations:

$$\sin \varepsilon = \frac{A_1 \cos \theta_{i+l}(z, t_6)}{\rho_i(z, t_3)}, \quad (25)$$

and

$$\begin{aligned} C_6^{i+l}P_3^i &= \cos(\theta_{i+l}(z, t_6) + \varepsilon) \frac{\rho_i(z, t_3)}{\cos \theta_{i+l}(z, t_6)} \\ &= \rho_i(z, t_3) [\cos \varepsilon - \sin \varepsilon \tan \theta_{i+l}(z, t_6)] \\ &= \rho_i(z, t_3) \left[ \sqrt{1 - \frac{A_1^2 \cos^2 \theta_{i+l}(z, t_6)}{\rho_i^2(z, t_3)}} - \frac{A_1 \sin \theta_{i+l}(z, t_6)}{\rho_i(z, t_3)} \right]. \end{aligned} \quad (26)$$

Substituting Eq. (26) into Eq. (23), and simplifying, we can write:

$$\begin{aligned} h_{tro}(z, t) &= \rho_{i+l}(z, t_6) + A_1 \sin \theta_{i+l}(z, t_6) \\ &\quad - \sqrt{\rho_i^2(z, t_3) - A_1^2 \cos^2 \theta_{i+l}(z, t_6)}. \end{aligned} \quad (27)$$

For convenience, the unknown terms in the right side of Eq. (27) are to be determined as functions of the local radius and immersion angle. Taking a vertical projection of  $P_6^{i+l}C_6^{i+l}$  and  $P_6^{i+l}O_6$  along the dotted line  $O_6C_6^{i+l}$  (shown in Fig. 8) we can derive that  $\rho_{i+l}(z, t_6) \sin \theta_{i+l}(z, t_6) = r + R_{i+l}(z) \sin \varphi_{i+l}(z, t_6)$ , from which we obtain:

$$\theta_{i+l}(z, t_6) = \sin^{-1} \left\{ \frac{r + R_{i+l}(z) \sin \varphi_{i+l}(z, t_6)}{\rho_{i+l}(z, t_6)} \right\}. \quad (28)$$

In  $\Delta C_6^{i+l}P_6^{i+l}O_6$  (see Fig. 8), using the cosine rule we can evaluate:

$$\rho_{i+l}(z, t_6) = \sqrt{r^2 + R_{i+l}^2(z) + 2rR_{i+l}(z) \cos \varphi_{i+l}(z, t_6)}. \quad (29)$$

Similarly in  $\Delta C_3^iP_3^iO_3$  (see Fig. 8), using again the cosine rule we can show:

$$\rho_i(z, t_3) = \sqrt{r^2 + R_i^2(z) + 2rR_i(z) \cos \varphi_i(z, t_3)}. \quad (30)$$

Having obtained expressions for all unknown in Eq. (27) in terms of the local radius and immersion angle, but for  $A_1$ ,  $A_1$  can be evaluated by first evaluating  $A_2$ . From Fig. 8, it is clear that the delay time  $\tau_{i,l}$  can be between  $t_1$  and  $t_4$  or between  $t_5$  and  $t_7$ . Hence we obtain  $P_1^iP_4^{i+l} = O_1O_4 = P_5^iP_7^{i+l} = O_5O_7 = f_{i,l}(z, t) = A$ . Now, in the time gap between  $t_1$  and  $t_2$ , the tool center moves by  $O_1O_2$  and the  $i^{th}$  flute rotates by  $\varphi_i(z, t_2)$  which is measured at  $O_2$ . Hence we obtain  $O_1O_2 = r\varphi_i(z, t_2)$ . Similarly  $O_1O_3 = r\varphi_i(z, t_3)$  and  $O_4O_6 = r\varphi_{i+l}(z, t_6)$ . In the time gap between  $t_2$  and  $t_4$ , the tool center moves by  $O_2O_4$  denoted by  $A_2$  in Fig. 8.  $A_2$  can hence be written as follows:

$$A_2 = O_2O_4 = (O_1O_4 - O_1O_2) = f_{i,l}(z, t) - r\varphi_i(z, t_2). \quad (31)$$

Similarly, in the time gap between  $t_3$  and  $t_6$ , the tool center moves by  $O_3O_6$  denoted by  $A_1$  in Fig. 8.  $A_1$  can hence similarly be evaluated as:

$$\begin{aligned} A_1 &= O_3O_6 = (O_1O_4 - O_1O_3) + O_4O_6 \\ &= f_{i,l}(z, t) - r\varphi_i(z, t_3) + r\varphi_{i+l}(z, t_6). \end{aligned} \quad (32)$$

Having obtained all the terms in the right hand side of Eq. (27), as desired, to further simplify, we find the relation between  $\varphi_{i+l}(z, t_j)$  and  $\varphi_i(z, t_i)$  by assuming  $\xi = \varphi_i(z, t_i) - \varphi_{i+l}(z, t_j)$ , wherein the index  $j$  that belongs to the  $(i+l)^{th}$  path, is linked to the index  $i$  that belongs to the  $i^{th}$  path by such way that when  $i=2, 3$  and  $5$  then the corresponding values of  $j=4, 6$  and  $7$ . As the tooth proceeds along its trochoidal path, the angle  $\xi$  varies. At the start of the engagement,  $\varphi_{i+l}(z, t_j) = \varphi_{i+l}(z, t_4) = 0$ ,  $\varphi_i(z, t_i) = \varphi_i(z, t_2)$  and  $\xi = \varphi_i(z, t_2)$ . At an intermediate time,  $\varphi_{i+l}(z, t_j) = \varphi_{i+l}(z, t_6)$ ,  $\varphi_i(z, t_i) = \varphi_i(z, t_3)$  and  $\xi = \gamma$  (shown in Fig. 8)  $= \varphi_i(z, t_3) - \varphi_{i+l}(z, t_6)$ . At exit of the engagement  $\varphi_{i+l}(z, t_j) = \varphi_{i+l}(z, t_7) \cong \frac{\pi}{2}$ ,  $\varphi_i(z, t_i) = \varphi_i(z, t_5) \cong \frac{\pi}{2}$  and  $\xi = 0$ . Therefore assuming a linear relation between  $\xi$  and  $\varphi_{i+l}(z, t_j)$  we determine the expression of  $\xi$  by linear interpolation as follows:

$$\xi = \varphi_i(z, t_2) \left( 1 - \frac{2\varphi_{i+l}(z, t_j)}{\pi} \right) = \varphi_i(z, t_i) - \varphi_{i+l}(z, t_j). \quad (33)$$

Rearranging Eq. (33) we obtain the relation between  $\varphi_{i+l}(z, t_j)$  and  $\varphi_i(z, t_i)$  as follows:

$$\varphi_{i+l}(z, t_j) = \frac{[\varphi_i(z, t_i) - \varphi_i(z, t_2)]}{\left[ 1 - \frac{2\varphi_{i+l}(z, t_2)}{\pi} \right]}, \quad (34)$$

wherein assuming very small angle,  $\varphi_i(z, t_2)$  (shown in Fig. 8) can be evaluated from Eq. (16) as follow:

$$\varphi_i(z, t_2) = \frac{f_{i,l}(z, t)}{r + R_i(z)}. \quad (35)$$

Using Eqs. (34) and (35) we can now express the term  $\varphi_{i+l}(z, t_6)$  of the Eq. (29) in term of  $\varphi_i(z, t_3)$ . Substituting Eqs. (28)–(32) into Eq. (27) we obtain an expression of  $h_{tro}(z, t)$  in terms of  $\varphi_i(z, t_3)$  as below:

In Eq. (36) the term  $\varphi_i(z, t_3)$  is an instantaneous angle at a general position, hence it can be replaced by  $\varphi_i(z, t)$ . Further simplifying Eq. (36) we finally obtain the following compact form for the relative radial distance between two corresponding trochoidal trajectories along the radius of curvature as:

$$h_{tro}(z, t) = \frac{[V + A_1(r + R_{i+l}(z)\sin W)]}{V^{0.5}} - \left[ V - \frac{A_1^2(R_{i+l}^2(z)\cos^2 W + 2\sqrt{2}rR_{i+l}(z)\cos(W + \frac{\pi}{4}))}{V} \right]^{1/2}, \quad (37)$$

wherein

$$\left. \begin{aligned} W &= \left[ \frac{\varphi_i(z, t) - \frac{f_{i,l}(z, t)}{r + R_i(z)}}{1 - \frac{2f_{i,l}(z, t)}{\pi(r + R_i(z))}} \right] \\ A_1 &= f_{i,l}(z, t) - r\varphi_i(z, t) + rW \\ V &= r^2 + R_{i+l}^2(z) + 2rR_{i+l}(z)\cos W \end{aligned} \right\}. \quad (38)$$

Substituting Eqs. (37) and (38) into Eq. (22) we finally determine the geometric static chip thickness  $h_{g,tro}^{st}(z, t)$  for serrated cutters considering trochoidal trajectories followed by the tool teeth. This however, does not signify the actual physical chip thickness. Elemental physical static chip thickness is calculated by multiplying two screening functions as follows:

$$h_i^{st}(z, t) = g_i(z, t)h_{g,tro}^{st}(z, t), \quad (39)$$

wherein,  $g_i(z, t) = g_{ri,i}(z, t)g_{h,i}(z, t)$ , is the product of the screening function due to radial immersion:

$$g_{ri,i}(z, t) = \begin{cases} 1, & \text{if } \varphi_{en} \leq (\varphi_i(z, t) \bmod 2\pi) \leq \varphi_{ex} \\ 0, & \text{otherwise} \end{cases} \quad (40)$$

$$\begin{aligned} h_{tro}(z, t) = & \sqrt{r^2 + R_{i+l}^2(z) + 2rR_{i+l}(z)\cos\left[\frac{\varphi_i(z, t_3) - \frac{f_{i,l}(z, t)}{r + R_i(z)}}{1 - \frac{2f_{i,l}(z, t)}{\pi(r + R_i(z))}}\right]} \\ & + \left( f_{i,l}(z, t) - r\varphi_i(z, t_3) + r\left[\frac{\varphi_i(z, t_3) - \frac{f_{i,l}(z, t)}{r + R_i(z)}}{1 - \frac{2f_{i,l}(z, t)}{\pi(r + R_i(z))}}\right] \right) \times \frac{\left( r + R_{i+l}(z)\sin\left[\frac{\varphi_i(z, t_3) - \frac{f_{i,l}(z, t)}{r + R_i(z)}}{1 - \frac{2f_{i,l}(z, t)}{\pi(r + R_i(z))}}\right] \right)}{\sqrt{r^2 + R_{i+l}^2(z) + 2rR_{i+l}(z)\cos\left[\frac{\varphi_i(z, t_3) - \frac{f_{i,l}(z, t)}{r + R_i(z)}}{1 - \frac{2f_{i,l}(z, t)}{\pi(r + R_i(z))}}\right]}} \\ & - \left\{ r^2 + R_i^2(z) + 2rR_i(z)\cos\varphi_i(z, t_3) - \left( f_{i,l}(z, t) - r\varphi_i(z, t_3) + r\left[\frac{\varphi_i(z, t_3) - \frac{f_{i,l}(z, t)}{r + R_i(z)}}{1 - \frac{2f_{i,l}(z, t)}{\pi(r + R_i(z))}}\right] \right)^2 \right. \\ & \times \left. \left( \frac{R_{i+l}^2(z)\cos^2\left[\frac{\varphi_i(z, t_3) - \frac{f_{i,l}(z, t)}{r + R_i(z)}}{1 - \frac{2f_{i,l}(z, t)}{\pi(r + R_i(z))}}\right] + 2rR_{i+l}(z)\left(\cos\left[\frac{\varphi_i(z, t_3) - \frac{f_{i,l}(z, t)}{r + R_i(z)}}{1 - \frac{2f_{i,l}(z, t)}{\pi(r + R_i(z))}}\right] - \sin\left[\frac{\varphi_i(z, t_3) - \frac{f_{i,l}(z, t)}{r + R_i(z)}}{1 - \frac{2f_{i,l}(z, t)}{\pi(r + R_i(z))}}\right]\right)}{\left( r^2 + R_{i+l}^2(z) + 2rR_{i+l}(z)\cos\left[\frac{\varphi_i(z, t_3) - \frac{f_{i,l}(z, t)}{r + R_i(z)}}{1 - \frac{2f_{i,l}(z, t)}{\pi(r + R_i(z))}}\right] \right)} \right)^{1/2} \end{aligned} \quad (36)$$

and, the screening function due to missed cut effect:

$$g_{h,i}(z, t) = \begin{cases} 1, & \text{if } h_{g, tro}^{st}(z, t) \geq 0 \\ 0, & \text{otherwise} \end{cases} \quad (41)$$

The calculation of exit angle ( $\varphi_{ex}$ ) and entry angle ( $\varphi_{en}$ ) defined in Eq. (40) is discussed in the next section.

When the geometric chip thickness (see Eq. (27)) becomes negative due to the inclusion of variation of local radius in chip thickness, then those corresponding flute(s) do not cut the surface because resultant movement of cutter occurs in backward direction. This is called the missed cut effect which causes non-uniform chip thickness, and can also be understood from Fig. 9. In Fig. 9 the next surface to be cut made by the  $(i + l)^{th}$  flute lags behind the current surface made by the  $i^{th}$  flute and hence a missed cut occurs. The irregular chip distribution caused by missed-cut-effect of serrated cutters produces periodic cutting forces with non-uniform amplitudes, which contributes to a reduction in instantaneous cutting forces, as discussed in the subsequent section.

#### Updated entry and exit angles

Due to actual trochoidal tool path and the influence of run-out, the local entry and exit angles for the serrated cutter are changed. The refined exit angle ( $\varphi_{ex}$ ) made at the point  $P_i$  is shown in Fig. 10 for up-milling case. The dashed line in Fig. 10 is made by the next  $(i + l)^{th}$  tooth and the solid line path is made by the current  $i^{th}$  tooth.

During the delay time  $\tau_{i,l}$ , radius of curvature of the serrated cutter moves from  $C^{i+l}$  to  $C^i$ . From Fig. 10 we get  $C^{i+l}P_{i+l} = \rho_{i+l}(z)$ ,  $C^iP_i = \rho_i(z)$ ,  $C^{i+l}C^i = f_{i,l}$  and the geometrical chip thickness  $h_{g, ie}^{st}(z, t) = P_iP_{i+l} \ll C^iP_i$ . Hence we obtain  $C^iP_{i+l} = C^iP_i - P_iP_{i+l} \approx C^iP_i = \rho_i(z)$ . Finally from  $\Delta C^{i+l}C^iP_{i+l}$  made of sides  $f_{i,l}$ ,  $\rho_i(z)$  and  $\rho_{i+l}(z)$ , the exit angle ( $\varphi_{ex}$ ) using the cosine rule can be shown to be:

$$\varphi_{ex} = \sin^{-1} \frac{[(\rho_{i+l}(z))^2 - (\rho_i(z))^2 - f_{i,l}^2(z, t)]}{2f_{i,l}(z, t)\rho_i(z)} \quad (42)$$

From Eq. (42) we observe that exit angle  $\varphi_{ex} := \varphi_{ex}^i(z)$  depends on the tooth and height of the serrated cutter considering run-out and trochoidal tool path. For the down-milling case, the entry

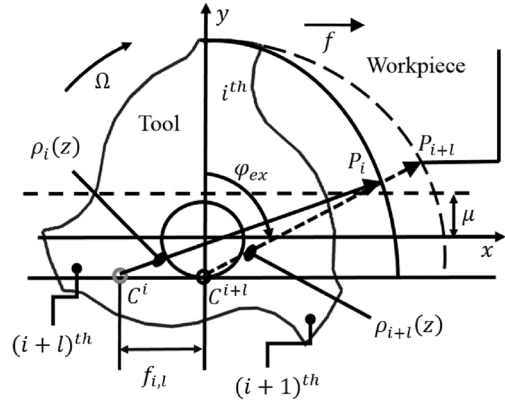


Fig. 10. Exit angle ( $\varphi_{ex}$ ) calculation for serrated end mill with run-out.

angle,  $\varphi_{en}$  is also modified as follows:

$$\varphi_{en} = \pi - \sin^{-1} \frac{[(\rho_{i+l}(z))^2 - (\rho_i(z))^2 - f_{i,l}^2(z, t)]}{2f_{i,l}(z, t)\rho_i(z)} \quad (43)$$

However, the effect of run-out on the updated entry and exit angles is negligible because the difference of local radius due to run-out is very small with respect to radial depth of cut. Hence, even though we present the updated formulations for these angles in Eqs. (42) and (43), these are ignored in the prediction of cutting forces.

#### Force model for serrated cutters

All differential elemental forces are calculated in each element of the discretized serrated tool with run-out as shown in Fig. 11.

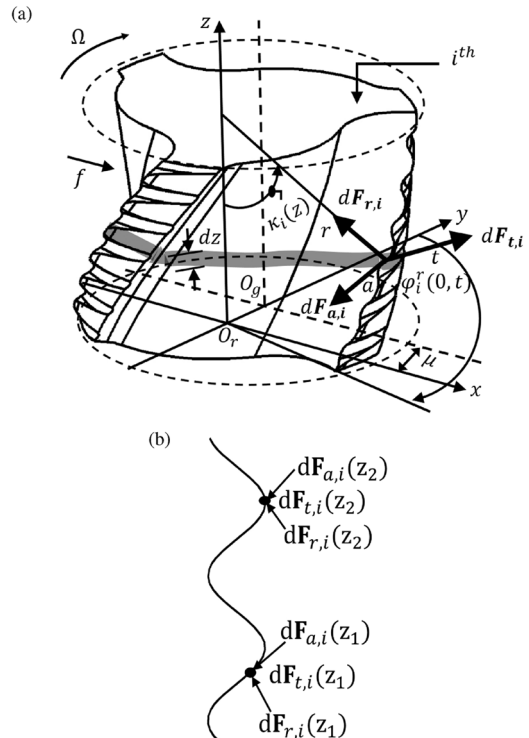


Fig. 11. (a) Differential forces acting on an infinitesimal  $dz$  axial segment on the  $i^{th}$  edge of the serrated cutter with run-out. (b) Variation of cutting force along flute and height.

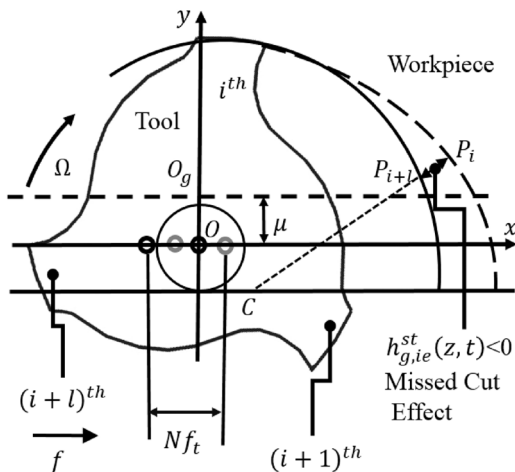


Fig. 9. Possible missed-cut effect of the serrated tool considering run-out.



The cutting forces for the  $i^{th}$  flute at a height  $z$  are found in the radial-tangential-and-axial, i.e.,  $rta$  directions as shown in Fig. 11a. Due to variation of the local tool geometry along the serration and along the axis of the tool, this  $rta$  frame changes its orientation as shown in Fig. 11b. Differential forces evaluated in the  $rta$  frame are given by:

$$d\mathbf{F}_{rta,i}(z, t) = \left[ \mathbf{K}^c h_i^{st}(z, t) + \mathbf{K}^e \right] \frac{dz}{\sin \kappa_i(z)} \mathbf{g}_i(z, t), \quad (44)$$

wherein primary cutting force coefficient vector is:

$$\mathbf{K}^c = \begin{bmatrix} K_r^c & K_t^c & K_a^c \end{bmatrix}^T \quad (45)$$

and, the edge cutting force coefficient vector is:

$$\mathbf{K}^e = \begin{bmatrix} K_r^e & K_t^e & K_a^e \end{bmatrix}^T. \quad (46)$$

These coefficients can either be identified mechanistically (as is done presently) for a given tool geometry and workpiece material combination, and for a given range of cutting conditions [36], or can be also obtained using an orthogonal to oblique transformation, from a given orthogonal database [37], as was done elsewhere in [15,16,19].

Differential forces evaluated in the  $rta$  frame are transformed to the fixed machine coordinate frame ( $xyz$ ) as follows:

$$d\mathbf{F}_{xyz,i}(z, t) = \mathbf{T}_{xr,i}(z, t) d\mathbf{F}_{rta,i}(z, t), \quad (47)$$

wherein the force transformation matrix is given by:

$$\mathbf{T}_{xr,i}(z, t) = \begin{bmatrix} -\sin \varphi_i \sin \kappa_i & -\cos \varphi_i & -\sin \varphi_i \cos \kappa_i \\ -\cos \varphi_i \sin \kappa_i & \sin \varphi_i & -\cos \varphi_i \cos \kappa_i \\ \cos \kappa_i & 0 & -\sin \kappa_i \end{bmatrix}, \quad (48)$$

with  $\varphi_i := \varphi_i(z, t)$ ,  $\kappa_i := \kappa_i(z)$ .

The total lumped cutting force vector acting on the cutting tool in the  $x$ ,  $y$  and  $z$  directions is calculated by integrating the differential force vector along flute and summing the contribution of all flutes as follows:

$$\mathbf{F}_{xyz}(t) = \begin{bmatrix} F_x & F_y & F_z \end{bmatrix}^T = \sum_{i=1}^N \int_0^{a_p} d\mathbf{F}_{xyz,i}(z, t). \quad (49)$$

This force model that incorporates an improved chip thickness model considering the trochoidal path traced by the cutter, and also includes the influence of run-out is used to predict cutting forces. We further contrast these forces with those predicted by the approximate circular path model and also with experimental results, as discussed next.

## Comparison of chip thickness and resultant forces



We discuss here the comparison of chip thickness predicted with the proposed improved model and the approximate model, and the corresponding resultant forces for both types of serrated cutters under investigations. Serration parameters for both cutters are listed in Table 1. These were measured on an Alicona make 3D surface profilometer. Cutting force coefficients used in the model were identified mechanistically on a 3 axis AMSL make CNC machine instrumented with a table top dynamometer as shown in Fig. 17. The run-out during measurements was inferred to be less than 5  $\mu\text{m}$ , and hence its influence on identification is ignored. Two materials were cut – Al7075, and a medium carbon steel. The Al7075 workpiece was cut with the 3-fluted serrated end mill that had a trapezoidal serration profile, and steel was cut with the 4-fluted serrated mill that had a circular serration profile. The identified coefficients are listed in Table 2.

Using the measured serration profiles and the coefficients, chip thickness and resultant forces in the  $x-y$  plane (i.e.,  $F_{xy} = \sqrt{F_x^2 + F_y^2}$ ) are compared in Figs. 12 and 13 for the trapezoidal profiled serrated cutter, and in Figs. 14 and 15 for the circular profiled serrated cutter. Comparisons are also made for the case of zero run-out and for a run-out of  $\mu = 30 \mu\text{m}$  and  $\delta = 30$ . Though investigations were carried out for a range of feeds and radial engagements, results in Figs. 12 and 14 are limited to only a representative subset of low feed ( $f = 0.02 \text{ mm/tooth/rev}$ ), and full immersion, i.e., slotting. A summary of comparisons for a range of operating conditions is made in Figs. 13 and 15.

## Comparisons for the trapezoidal profiled serrated cutter

Comparisons in Fig. 12 clearly show that the differences between the improved chip thickness model and the approximate chip thickness model are negligible, varying at most by 0.17%.

**Table 1**  
Geometry of the serrated cutters

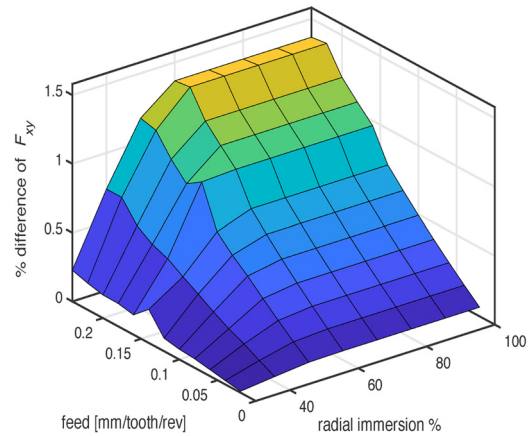
Serration profile	Tool diameter ( $D$ )	Serration Parameters	Initial phase shift ( $\psi$ )	No of flutes ( $N$ )	Helix angle ( $\eta$ )	Rake angle
Trapezoidal 	16	$A = 0.63 \text{ mm};$ $L_1 = 0.97 \text{ mm};$ $L_2 = 0 \text{ mm};$ $R_1 = 0.06 \text{ mm};$ $R_2 = 0.39 \text{ mm};$ $R_3 = 0.39 \text{ mm};$ $R_4 = 0.06 \text{ mm};$ $\alpha_{serr} = 39^\circ;$ $\beta_{serr} = 40^\circ;$ $\lambda = 2.82 \text{ mm}$	$[0 \ 120 \ 240]^\circ$	3	$40^\circ$	$10^\circ$
Circular 	16	$A_1 = 0.13 \text{ mm};$ $A_2 = 0.27 \text{ mm};$ $R_1 = 0.3 \text{ mm};$ $R_2 = 0.63 \text{ mm};$ $A = A_1 + A_2$ $= 0.4 \text{ mm};$ $\lambda = 1.5 \text{ mm}$	$[0 \ 90 \ 180 \ 270]^\circ$	4	$40^\circ$	$10^\circ$

**Table 2**  
Mechanically identified coefficients

Material cut	Identified coefficients					
	$K_r^c$ (N/mm <sup>2</sup> )	$K_r^e$ (N/mm <sup>2</sup> )	$K_a^c$ (N/mm <sup>2</sup> )	$K_t^e$ (N/mm)	$K_r^e$ (N/mm)	$K_a^e$ (N/mm)
Al7075	824	225	15	24	28	2
Steel	1925	437	−216	24	20	−9

These comparisons were made for slot cutting AL7075 at a depth of cut of 2 mm and at speed of 6000 rpm with a feed of 0.02 mm/tooth/rev. For the case with run-out included, see Fig. 12b the chip thickness distribution changes when compared to the case of no run-out in Fig. 12a. This change in the chip thickness distribution with run-out contributes to a change in the profile of the resultant cutting force in Fig. 12d when compared to the case of no run-out in Fig. 12c, however the difference in maximum forces remains negligible (as it is less than 1%). This suggests that the approximate circular chip thickness model remains valid, and that run-out too has a negligible influence on cutting forces for serrated cutters.

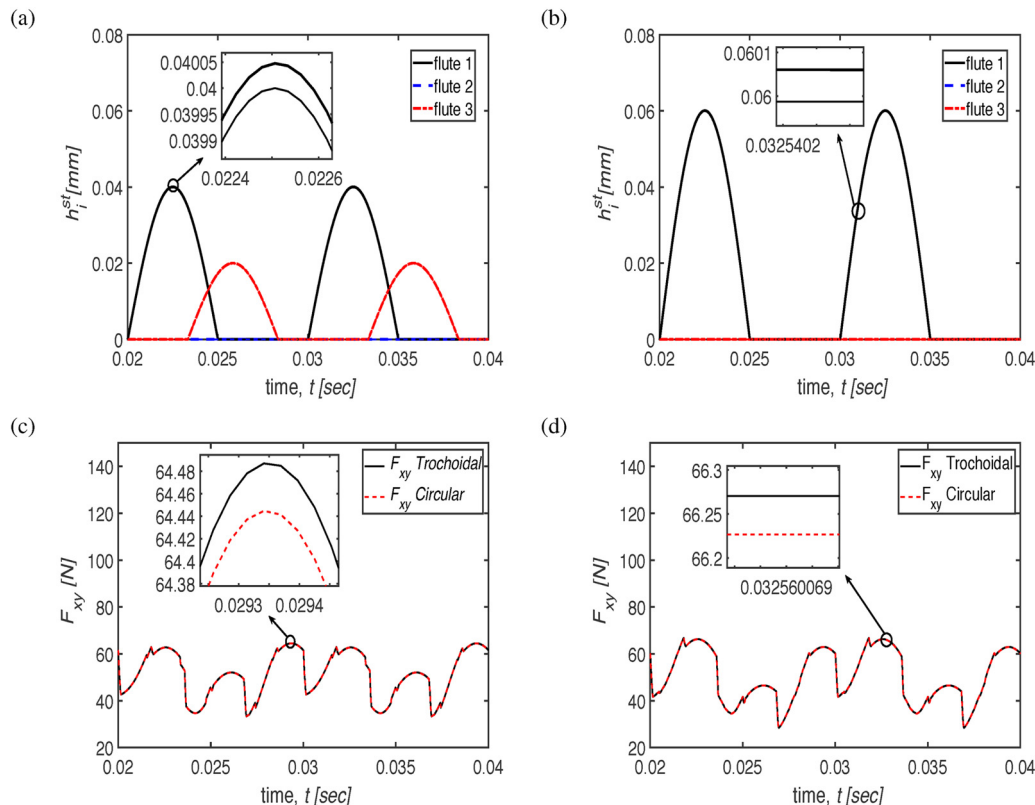
Since Fig. 12 shows results only for one level of feed and for slot cutting, differences between maximum resultant cutting forces due to the proposed improved chip profile and the approximate circular chip profile for a range of feeds (0.02–0.25 mm/tooth/rev) and radial engagements (30–100%) can be understood from Fig. 13. All results in Fig. 13 are for the case of no run-out. For a fixed engagement, the differences between the proposed model and the approximate model are observed to increase with feed rate, becoming at most ~1.4%, whereas for a fixed feed rate, differences in general increase with engagement, becoming also at most ~1.4%. These trends are true for chip thickness too. The observed

**Fig. 13.** Difference in maximum resultant cutting force with changing feed and radial immersion for the 3-fluted trapezoidal profiled serrated cutter with no run-out.

differences are consistent with those reported for regular end mills, elsewhere in [1,5].

#### Comparisons for the circular profiled serrated cutter

Similarly comparing the differences in chip thickness formulations with the circular profiled 4-fluted serrated cutter in Fig. 14 for slot cutting a medium carbon steel at a depth of cut of 2 mm and at speed of 1600 rpm with a feed of 0.02 mm/tooth/rev, we find the difference between both chip profiles is negligible, varying by at most 0.18%. And, as before, even though there is a change in the

**Fig. 12.** Comparison of chip thickness and forces for the 3-fluted trapezoidal profiled serrated cutter. (a) chip thickness at the tool tip with no run-out; (b) chip thickness at the tool tip with run-out. Trochoidal chip profile represented by thick lines, and circular approximation with thin lines. (c) resultant forces with no run-out; (d) resultant forces with run-out.

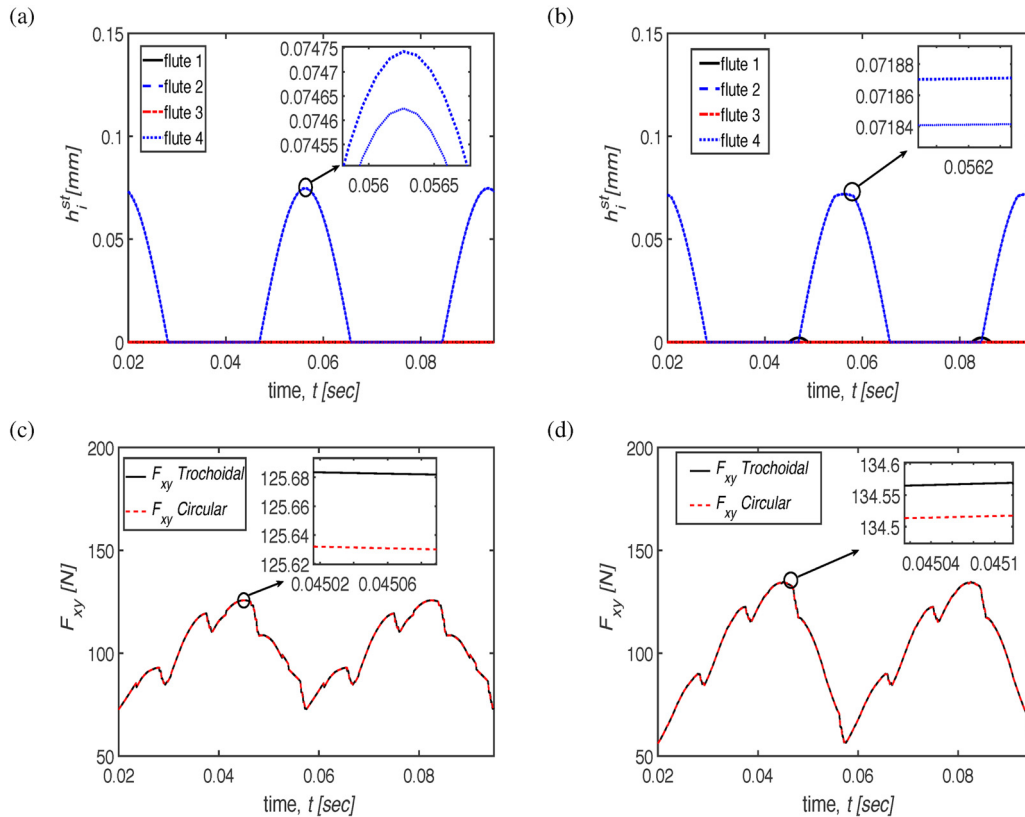


**Fig. 14.** Comparison of chip thickness and forces for the 4-fluted circular profiled serrated cutter. (a) chip thickness at the tool tip with no run-out; (b) chip thickness at the tool tip with run-out. Trochoidal chip profile represented by thick lines, and circular approximation with thin lines. (c) resultant forces with no run-out; (d) resultant forces with run-out.

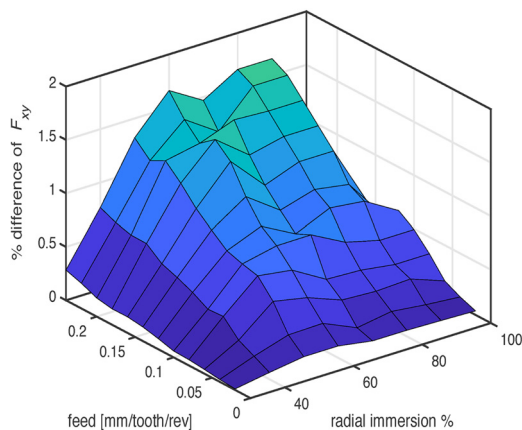


**Fig. 15.** Difference in maximum resultant cutting force with changing feed and radial immersion for the 4-fluted circular profiled serrated cutter with no run-out.

chip load distribution across the teeth for the case with run-out (see Fig. 14(a–b)), the change in the resultant cutting forces are negligible (see Fig. 14(c–d)). Furthermore, the summary of the differences for changing feeds and engagements, as shown in Fig. 15 for the case of no run-out is consistent with earlier observations, with the maximum difference observed to be  $\sim 1.7\%$ .

Our findings suggest that the approximate circular chip thickness model remains valid for serrated end milling, and that differences between maximum resultant cutting forces due to the proposed improved chip thickness model and the approximate model is maximum at high feed, which is consistent with the passing observations made in [13]. We also find that even a

moderate level of run-out on serrated cutters does not adversely change the chip load or the force profile. These model predicted observations are confirmed through experiments Section 6 after the discussion of run-out measurement. Section 6.

### Inferring run-out on serrated cutters from measurements

Since radial run-out results in a local change in the radius of the cutter, its effect is easy to confound with the change in the local radius on account of the serration geometry. To discern the change in radius due to run-out from that of the change in radius due to serration geometry, we infer radial run-out on serrated tools using a combination of measurements and scanned geometry of the serration profiles.

The run-out inference setup for the representative 3-flute trapezoidal serrated cutter is shown in Fig. 16(a). Local change in radius is measured using a dial gauge in static condition (zero rpm) at different levels. The schematic of measurement locations at different serration heights is shown in Fig. 16(b), and the corresponding cross-sectional views are shown in Fig. 16(c). Differences of rotational radius  $R_t(z)$  between different flutes at different heights are measured by a dial gauge probe, and the differences in geometrical radius  $R_t^g(z)$  between different flutes at different heights are evaluated from measurements on an Alicona make 3D surface profilometer.

The detailed procedure to infer the radial run-out is as under:

- At first, we measure the difference of local radius,  $R_t(z)$  between the three flutes at  $z=0$  mm (tool tip). The geometrical radius  $R_t^g(z)$  is the same for each flute at this location, being 8 mm, due to the initial land on the cutter, as shown in Fig. 16(b–c).

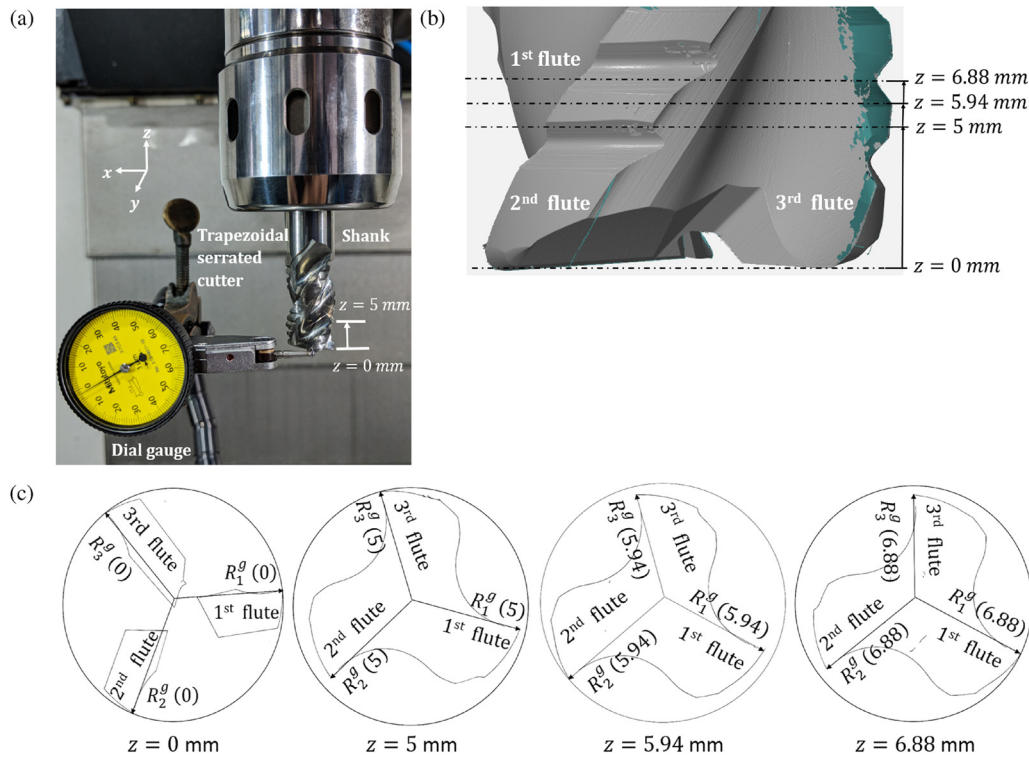


**Fig. 16.** (a) Run-out inference setup for 3-flute trapezoidal serrated cutter (b) schematic of measurement locations at different serration heights (c) Cross-sectional views of the serrated cutter at corresponding axial heights.

- We then measure the local radius at the  $z = 5 \text{ mm}$  location. We deliberately choose this location since the third flute on this three flute cutter has an upper land at this location, and the geometrical radius,  $R_1^g(z) = 8 \text{ mm}$ . At this same location, the first and the second flutes have a geometrical radius,  $R_i^g(z) < 8 \text{ mm}$  – as is evident from Fig. 16(b–c), and since the diameter of dial gauge probe is of the order of length (width) of the trough, measurement of the local radius of the first and second flute at this location is not feasible.
- Since we can measure the local radius only at the sections on the flutes where there is an upper land, and because this is a three fluted cutter with serration profiles phase shifted in a regular manner, i.e., with a phase shift of  $[0 \ 120 \ 240]^\circ$ , we next measure the local radius of the second flute where there is an upper land, i.e., at the  $z = 5 + \lambda/3 = 5.94 \text{ mm}$ , and where the first flute has an upper land, i.e., at the  $z = 5 + 2\lambda/3 = 6.88 \text{ mm}$  locations, wherein  $\lambda$  is the wavelength of the trapezoidal serration.

- We next measure the radius on the cylindrical shank part of the tool. All measurements are tabulated in Table 3.

Substituting these measured values into Eq. (3), we calculate the run-out parameters,  $\mu$  (radial deviation) and  $\delta$  (run-out angle). Evaluated parameters are also listed in Table 3.

Though the above described procedure is specific to the three-fluted trapezoidal serrated end mill, it can be easily generalized. The axial locations where local radius is to be measured depends on the number of flutes and initial phase shift of serrations. For instance, for a four-fluted serrated cutter with a regular phase shift of  $[0 \ 90 \ 180 \ 270]^\circ$ , locations from the upper land of the first flute, will be indexed by  $\lambda/4$ ,  $2\lambda/4$  and  $3\lambda/4$ , for the second, third, and fourth flutes respectively.

From the Table 3 we see the value of  $\mu$  is  $1 \mu\text{m}$  which is very low and constant throughout the axial height, i.e., rotational and geometrical axis are parallel which means there is no axial tilt.

**Table 3**  
Inferred run-out parameters for three-fluted trapezoidal serrated cutter

Positions	Difference of rotational radius $R_i(z)$ between different flutes at different heights measured by dial gauge probe	Difference of geometrical radius $R_i^g(z)$ between different flutes at different heights measured by Alicona 3D	Identified $\mu$ and $\delta$
$z = 0 \text{ mm}$ (initial land portions, i.e., non-serrated part)	$\Delta_1 = R_1(0) - R_2(0) = 1 \mu\text{m}$ , $\Delta_2 = R_2(0) - R_3(0) = 1 \mu\text{m}$ , $\Delta_3 = R_3(0) - R_1(0) = -2 \mu\text{m}$	$\Delta_1^g = R_1^g(0) - R_2^g(0) = (8 - 8) \text{ mm} = 0 \text{ mm}$ , $\Delta_2^g = R_2^g(0) - R_3^g(0) = (8 - 8) \text{ mm} = 0 \text{ mm}$ , $\Delta_3^g = R_3^g(0) - R_1^g(0) = (8 - 8) \text{ mm} = 0 \text{ mm}$	$\mu = 1 \mu\text{m}$ , $\delta = 33^\circ$
Measured at $z = 5 \text{ mm}$ for 3 <sup>rd</sup> flute, at $z = 5 + \lambda/3 = 5.94 \text{ mm}$ for 2 <sup>nd</sup> flute, at $z = 5 + 2\lambda/3 = 6.88 \text{ mm}$ for 1 <sup>st</sup> flute (at upper lands of serrated part)	$\Delta_1 = R_3(5) - R_2(5.94) = 0 \mu\text{m}$ , $\Delta_2 = R_2(5.94) - R_1(6.88) = -1 \mu\text{m}$ , $\Delta_3 = R_1(6.88) - R_3(5) = 1 \mu\text{m}$	$\Delta_1^g = R_3^g(5) - R_2^g(5.94) = (8 - 8) \text{ mm} = 0 \text{ mm}$ , $\Delta_2^g = R_2^g(5.94) - R_1^g(6.88) = (8 - 8) \text{ mm} = 0 \text{ mm}$ , $\Delta_3^g = R_1^g(6.88) - R_3^g(5) = (8 - 8) \text{ mm} = 0 \text{ mm}$	$\mu = 1 \mu\text{m}$ , $\delta = 33^\circ$
Shank	–	–	$\mu = 1 \mu\text{m}$



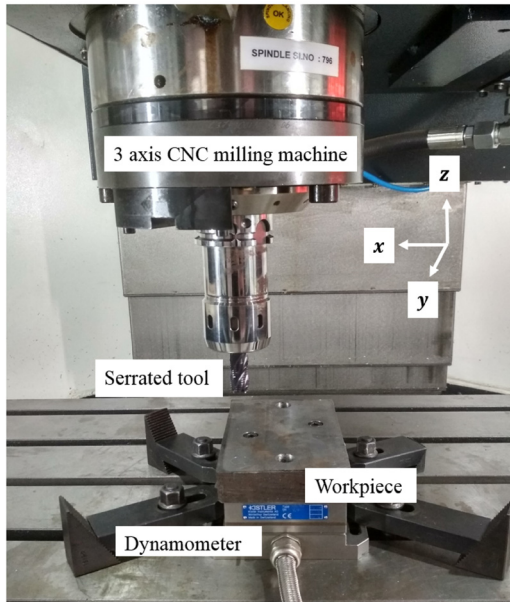


Fig. 17. Experimental validation of cutting forces.

Hence we have neglected run-out in the experimental validation as it is less than  $5\ \mu\text{m}$  for both tools. We also ignore any dynamic run-out influences, if present.

### Experimental validation of cutting forces

Model predicted forces for both types of chip thickness profiles for both types of serrated cutters under investigation are

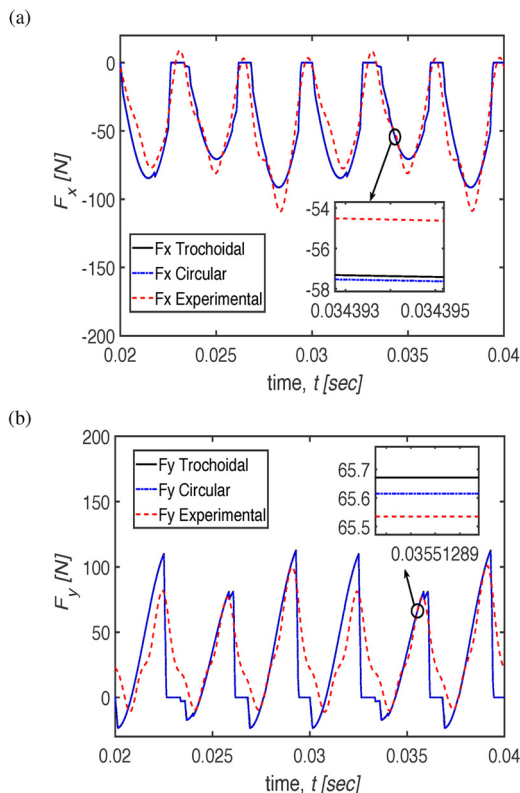


Fig. 18. Experimental validation of (a)  $F_x$  and (b)  $F_y$  using the 3-fluted trapezoidal serrated cutter for cutting Al7075.

experimentally validated using the setup as described earlier, and as shown in Fig. 17. Measured forces were low-pass filtered, and these forces are compared with model predictions in Figs. 18 and 19. Both cutters were mounted in a power-milling-chuck type holder, and the measured run-out at the tool tip was observed to be less than  $5\ \mu\text{m}$ , and since run-out was observed to be insignificant, it was ignored presently in the models for comparison with experiments.

Since serrated cutters are more effective at low feeds than at high, sample results for low feed cutting are shown in Figs. 18 and 19 for the 3-fluted trapezoidal profiled serrated cutter and the 4-fluted circular profiled serrated cutter, respectively. As before, Al7075 was cut with the 3-fluted cutter and medium carbon steel with the 4-fluted cutter. Al7075 was cut with a depth of cut of 2 mm at a speed of 6000 rpm in the 50% up-milling mode with a feed of 0.05 mm/tooth/rev. And, steel was cut in the 50% down-milling mode with a depth of cut of 2 mm at a speed of 1600 rpm with a feed of 0.05 mm/tooth/rev.

As is evident from the comparisons in Figs. 18 and 19, the difference between forces predicted with the proposed improved chip thickness model and the approximate chip thickness model remain negligible, and both compare very well with the experimentally measured forces. This confirms our model based investigations shown earlier. Even though the proposed model is complete and more representative of the actual cutting taking place, the circular chip thickness model is indeed a reasonable approximation for predicting cutting forces with serrated cutters.

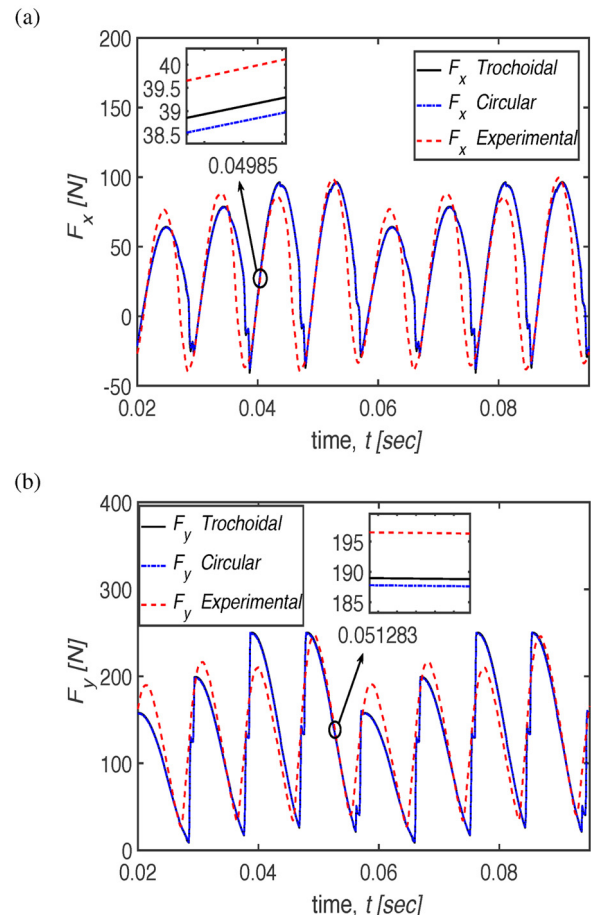


Fig. 19. Experimental validation of (a)  $F_x$  and (b)  $F_y$  using the 4-fluted circular serrated cutter for cutting steel.

## Conclusion

A comprehensive geometric model for chip thickness that traces the actual trochoidal path followed by milling cutters was presented for serrated tools. The model factored in the influence of radial run-out on the chip thickness distribution. We also presented a method to infer radial run-out on serrated tools using a combination of measurements and scanned geometry of the serration profiles. Though we ignored axial run-out in our model, from radial run-out inference, we figured that for low levels of radial run-out, the axial run-out is negligible, and hence does not adversely influence our model. Even though we limited our investigations in this paper to serrations only of the trapezoidal and circular kind, models presented are generalized, and can be extended to serrated cutters with different geometries.

Detailed analysis of the proposed improved chip thickness model and its influence on forces was presented for a range of cutting feeds and engagements, for cutting of Aluminum and steel, at different speeds. We observed that the difference between cutting forces due to the proposed trochoidal chip thickness and the circular approximation in general increase with feed and radial engagements. The difference however was observed to be negligible, with the maximum difference being at most 2%. This was supported by experiments. For run-outs of the order of feed 0.02 – 0.05 mm/tooth/rev, or less, we further observed that cutting force profiles and levels were not significantly altered, changing at most by 1%, suggesting that serrated cutters may be used even with moderate levels of run-outs when the feed is low.

Even though the proposed model is complete and more representative of the actual cutting taking place, we conclude that the circular chip thickness model is indeed a reasonable approximation for predicting cutting forces with serrated cutters. Our results can instruct the design and use of the next-generation of serrated cutters that preferentially reduce cutting forces and make easier the high-performance machining of difficult-to-cut materials across industries.

## Acknowledgements

We gratefully acknowledge support from Forbes & Company Limited, India in helping with geometric measurements on their profilometer. We also acknowledge the support from the Government of India's Impacting Research Innovation and Technology (IMPRINT) initiative through project number IMPRINT 5509.

## References

- [1] Martellotti, M., 1941, An analysis of the milling process. *Trans ASME*, 82/63: 677–700.
- [2] Martellotti, M.E., 1945, An Analysis of the Milling Process, Part II - Down Milling. *Trans Am Soc Mech Eng*, 67:233–251.
- [3] Spiewak, S., 1994, Analytical modeling of cutting points trajectories in milling. *J Ind Eng*, 116:440–448.
- [4] Spiewak, S., 1995, An Improved Model of the Chip Thickness in Milling. *CIRP Ann - Manuf Technol*, 44/1: 39–42.
- [5] Li, H.Z., Liu, K., Li, X.P., 2001, A new method for determining the undeformed chip thickness in milling. *J Mater Process Technol*, 113/1–3: 378–384.
- [6] Kumanchik, L.M., Schmitz, T.L., 2007, Improved analytical chip thickness model for milling. *Precis Eng*, 31/3: 317–324.
- [7] Kline, W.A., DeVor, R.E., 1983, The effect of runout on cutting geometry and forces in end milling. *Int J Mach Tool Des Res*, 23/213: 123–140.
- [8] You, S.J., Ehmann, K.F., 1991, Synthesis and Generation of Surfaces Milled by Ball Nose End Mills Under Tertiary Cutter Motion. *ASME J Eng Ind*, 113:17–24.
- [9] Montgomery, D., Altintas, Y., 1991, Mechanism of Cutting Force and Surface Generation in Dynamic Milling. *J Eng Ind*, 113/2: 160.
- [10] Altintas, Y., Montgomery, D., Budak, E., 1992, Dynamic peripheral milling of flexible structures. *J Eng Ind Trans ASME*, 114/2: 137–145.
- [11] Sahoo, P., Patra, K., 2018, Mechanistic modeling of cutting forces in micro-end-milling considering tool run out, minimum chip thickness and tooth overlapping effects. *Mach Sci Technol*, 0344:1–24.
- [12] Tlustý, J., Ismail, F., Zaton, W., 1983, Use of Special Milling Cutters against Chatter. *Proceedings of the NAMRC11 (University of Wisconsin SME)*, 408–415.
- [13] Campomanes, M.L., 2002, Kinematics and dynamics of milling with roughing tools, *Metal Cutting and High Speed Machining*. Kluwer Academic Publishers Plenum Press, Dordrecht, New York: 129–140. 2002 Apr 1.
- [14] Wang, J.J., Yang, C.S., 2003, Angle and frequency domain force models for a roughing end mill with a sinusoidal edge profile. *Int J Mach Tools Manuf*, 43:1509–1520.
- [15] Merdol, S.D., Altintas, Y., 2004, Mechanics and dynamics of serrated cylindrical and tapered end mills. *J Manuf Sci Eng*, 126/2: 317.
- [16] Dombovari, Z., Altintas, Y., Stepan, G., 2010, The effect of serration on mechanics and stability of milling cutters. *Int J Mach Tools Manuf*, 50/6: 511–520.
- [17] Hosseini, B., Moetakef-Imani, A., Kishawy, H.A., 2010, Mechanistic modelling for cutting with serrated end mills - a parametric representation approach. *Proceedings of the Institution of Mechanical Engineers Part B Journal of Engineering Manufacture*, 225:1019–1032.
- [18] Kaymakci, M., Kilic, Z.M., Altintas, Y., 2012, Unified cutting force model for turning, boring, drilling and milling operations. *Int J Mach Tools Manuf*, 54-55:34–45.
- [19] Koca, R., Budak, E., 2013, Optimization of serrated end mills for reduced cutting energy and higher stability. *Procedia CIRP*, 8:570–575.
- [20] Tehranizadeh, F., Budak, E., 2017, Design of serrated end mills for improved productivity. *Procedia CIRP*, 58:493–498.
- [21] Zheng, H.Q., Li, X.P., Wong, Y.S., Nee, A.Y., 1999, Theoretical modelling and simulation of cutting forces in face milling with cutter runout. *Int J Mach Tools Manuf*, 39/12: 2003–2018.
- [22] Wan, M., Zhang, W.H., Dang, J.W., Yang, Y., 2009, New procedures for calibration of instantaneous cutting force coefficients and cutter runout parameters in peripheral milling. *Int J Mach Tools Manuf*, 49/14: 1144–1151.
- [23] Krüger, M., Denkena, B., 2013, Model-based identification of tool runout in end milling and estimation of surface roughness from measured cutting forces. *Int J Adv Manuf Technol*, 65/5–8: 1067–1080.
- [24] T. L. Schmitz, J. Couey, E. Marsh, N. Mauntler, D. Hughes, Runout effects in milling: Surface finish, surface location error, and stability, *International Journal of Machine Tools and Manufacture* 47 (5 SPEC. ISS.) (2007) 841–851.
- [25] Li, Z.L., Niu, J.B., Wang, X.Z., Zhu, L.M., 2015, Mechanistic modeling of five-axis machining with a general end mill considering cutter runout. *Int J Mach Tools Manuf*, 96:67–79.
- [26] Wojciechowski, S., Chwalczuk, T., Twardowski, P., Krolczyk, G.M., 2015, Modeling of cutter displacements during ball end milling of inclined surfaces. *Archiv Civil Mech Eng*, 15/4: 798–805.
- [27] Wojciechowski, S., Wiackiewicz, M., Krolczyk, G.M., 2018, Study on metrological relations between instant tool displacements and surface roughness during precise ball end milling. *Measurement*, 129:686–694.
- [28] Wang, J.J., Zheng, C.M., 2003, Identification of cutter offset in end milling without a prior knowledge of cutting coefficients. *Int J Mach Tools Manuf*, 43/7: 687–697.
- [29] Hekman, K.A., Liang, S.Y., 1997, In-process monitoring of end milling cutter runout. *Mechatronics*, 7/1: 1–10.
- [30] Lee, K.Y., Kim, H.M., Park, S.S., 2007, A run-out measuring method using modeling and simulation in four-fluted end milling. *J Mater Process Technol*, 187-188:207–211.
- [31] P. Bari, P. Wahi, M. Law, Investigations on the Influence of Serration Parameters on Cutting Forces, *Proceedings of the AIMTDR 2018*, Anna University, Chennai, India (to appear).
- [32] P. Bari, M. Law, P. Wahi, Investigations on the influence of radial run-out on cutting forces for serrated cutters, *Proceedings of the ICCMM 2019 - IIT Guwahati*, India (to appear).
- [33] Kaczmarek, J., 1976, Principles of machining by cutting, abrasion and erosion. Peter Peregrinus Ltd.
- [34] M. Conroy, A cycloid (a common trochoid) generated by a rolling circle (2007). URL <https://en.wikipedia.org/wiki/Trochoid#/media/File:CycloidAnim04.gif>.
- [35] Miller, W., 2007, The Formula for Curvature. *Notes in IT Calculus II*, 2/1: 2–4.
- [36] Altintas, Y., 2001, *Manufacturing Automation: Metal Cutting Mechanics, Machine Tool Vibrations, and CNC Design*, Vol. 54.
- [37] Budak, E., Altintas, Y., Armarego, E.J.A., 1996, Prediction of ball-end milling forces from orthogonal cutting data. *Int J Mach Tools Manuf*, 36/9: 1059–1072.